The electromagnetic Brillouin precursor in one-dimensional photonic crystals

Uitham, R.; Hoenders, B. J.

Published in:
Optics Communications

DOI:
10.1016/j.optcom.2008.07.064

Publication date:
2008

Optics Communications 281 (2008) 5910–5918

Contents lists available at ScienceDirect

Optics Communications

journal homepage: www.elsevier.com/locate/optcom

The electromagnetic Brillouin precursor in one-dimensional photonic crystals

R. Uitham *, B.J. Hoenders

Zernike Institute for Advanced Materials, University of Groningen, Nijenborgh 4, 9747 AG Groningen, The Netherlands

ARTICLE INFO

Article history:
Received 19 December 2007
Received in revised form 22 April 2008
Accepted 25 July 2008

ABSTRACT

We have calculated the electromagnetic Brillouin precursor that arises in a one-dimensional photonic crystal that consists of two homogeneous slabs which each have a single electron resonance. This forerunner is compared with the Brillouin precursor that arises in a homogeneous double-electron resonance medium. In both types of medium, the precursor consists of the components of the applied pulse that have their frequencies below the lowest of the two electron resonances. In the inhomogeneous medium however, the slab contrast starts affecting the precursor field after a certain rise time of the precursor: its spectrum starts to peak at the geometric scattering resonances of the medium whereas minima appear at the Bragg-scattering frequencies.

1. Introduction

In 1914, Sommerfeld and Brillouin [1] published a paper on electromagnetic pulse propagation in spatially homogeneous, temporally dispersive media. With the method of steepest descent, they calculated that during the propagation of optical electromagnetic pulses in dielectric, nonmagnetic Lorentz media with a single electron resonance, two different electromagnetic precursors evolve, propagating ahead of the main part of the pulse. These forerunners have been experimentally observed for the first time in 1969 by Pleshko and Palócz [2]. The fastest propagating one is the Sommerfeld precursor. This forerunner arises from the very high-frequency components of the applied pulse, where very high means as compared to the single electron resonance frequency of the homogeneous medium. For these high frequencies, the response of the medium to the field very much resembles that of a vacuum, which explains the rapid propagation and slow decay of this first precursor. The wavefront of the Sommerfeld precursor propagates exactly at the vacuum speed of light. Behind the Sommerfeld precursor follows the Brillouin precursor. This forerunner arises from the very low-frequency components of the applied pulse, where low frequency again means as compared to the electron resonance frequency. These components interact relatively weak with the medium as well. After the Brillouin precursor, the main part of the applied pulse follows.

It is our aim to describe pulse propagation in photonic crystals [3] and in this paper, we extrapolate the Brillouin precursor theory from homogeneous media to a one-dimensional photonic crystal, modeled as a stratified multiple-layer medium. In a previous paper [13], we have already calculated the transmitted Sommerfeld precursor in such a medium. There we found that this precursor merely feels the spatial average of the medium; we did not find any effects on the propagation and wave-shape of the Sommerfeld precursor from the fact that the medium is inhomogeneous. This could be understood because at the high frequencies of the Sommerfeld precursor, the contrast between the slabs in the medium is extremely small, because all slabs nearly respond as if they were a vacuum. From this point, it is to be expected that the Brillouin precursor will be influenced stronger by the medium inhomogeneities since the slab contrast does not vanish at the low frequencies.

In this paragraph we review photonic crystals. These materials have recently gained much interest, because they can control the propagation of light. A photonic crystal [3] is a spatially repeated geometrical structure, or unit cell, of various material compounds that each individually have in general a different interaction strength with an electromagnetic field so that a propagating electromagnetic field is reflected periodically. Exactly as in the case of electrons in interaction with a periodic atomic lattice, where a band-gap appears in the electron dispersion relation due to Bragg scattering, the lattice of material compounds in photonic crystals creates a band-gap for electromagnetic radiation. For the frequencies inside this gap, no propagating wave solutions exist inside the crystal. If the band-gap lies in the visible part of the spectrum, the photonic crystal is called an optical photonic crystal. Another interesting effect of photonic crystals is that the group velocity of an electromagnetic pulse can be reduced considerably [4,5] when the pulse is predominantly composed of frequencies that lie close to the edge of the band-gap [6]. Therefore photonic crystals open new avenues to manipulate the propagation of an electromagnetic field. The expected applications of photonic crystals that rely on the aforementioned properties are numerous, for instance: waveguides [3], diodes [7], data storage compounds [8], delay lines [8,9], lasers [11] and devices that control the spontaneous atomic emission of

* Corresponding author. Tel.: +31 50 363 4958.
E-mail address: r.uitham@rug.nl (R. Uitham).

0030-4018/$ - see front matter © 2008 Elsevier B.V. All rights reserved.
doi:10.1016/j.optcom.2008.07.064

photons [10,12]. However, it is still difficult to grow highly regular three-dimensional structures with lattice constants of only a few hundreds of nanometers so that the large-scale fabrication of three-dimensional optical photonic crystals is still limited.

This paper has been organized as follows. In Section 2, the photonic crystal is modeled and its transmission coefficient for the electromagnetic field is derived in Section 3. The transmittance of the medium is analyzed numerically in Section 4. Thereafter, in Section 5 we discuss how to apply the method of steepest descent in order to calculate the Brillouin precursor. Then, in Section 6, we calculate the transmitted Brillouin precursor resulting from a delta-peak input pulse and from a step-modulated sinusoidal input field. In Section 7 the results are discussed. Finally, conclusions are drawn in Section 8.

2. Model for the photonic crystal

Our model for the photonic crystal is a stratified one-dimensional multiple-layer medium which has been depicted in Fig. 1. The x-axis is taken as the principal axis of the medium. The crystal consists of N layers of physical width l and each layer contains two homogeneous slabs, denoted as slab A and slab B, respectively of physical widths l_A and l_B that add up to the layer width, $l_A + l_B = l$. The coordinates of the interfaces are given as

$$\begin{aligned} &x_{mn} = x_{\mathrm{L}} + (n-1)l + \delta_{mB} l_A, \quad m = A, B, \quad n = 1, \ldots, N, \\ &x_{\mathrm{R}} = x_{\mathrm{L}} + Nl. \end{aligned} \tag{1}$$

The interfaces at $x = x_{\mathrm{L}}$ and at $x = x_{\mathrm{R}}$ are respectively referred to as the entrance and exit interface. To the left and to the right from the N-layer medium there are respectively the homogeneous materials L and R. All homogeneous materials $m = A, B, L, R$ give an isotropic and linear response to the electromagnetic field so that these materials are fully characterized with the scalar permittivities and permeabilities. The response to the electric component of the field is modeled as that of a Lorentz medium with a single[1] electron resonance [1] whereas the medium does not interact with the magnetic component. The absolute permittivity and absolute permeability of medium m are therefore given by, respectively

$$\epsilon_m = \epsilon_0 + \frac{\epsilon_0 \omega_{pm}^2}{\omega_m^2 - 2\mathrm{i}\gamma_m \omega - \omega^2}, \tag{2a}$$

$$\mu_m = \mu_0, \tag{2b}$$

where ω is the angular frequency of the electromagnetic field, ϵ_0 and μ_0, respectively the vacuum permittivity and permeability, ω_m the electron resonance frequency, ω_{pm} the plasma frequency and γ_m the absorption parameter of medium m. Now that the photonic crystal has been modeled, its transmission coefficient for the amplitude of the electric component of an electromagnetic field will be calculated in the following section.

3. Transmission coefficient of the photonic crystal

We take a perpendicularly incident applied field. The theory allows for an extension to oblique incidence with separation in TE- and TM-polarization, but since we are only interested in the effect of the medium inhomogeneities, this extension would merely obscure the purpose of our paper. The system of the N-layer medium plus the two surrounding media consists of $2N + 2$ homogeneous parts, separated by sharp interfaces. The homogeneous subspaces are labeled as mn, where the first index $m = A, B, L, R$ indicates the material and the last index $n = 1,\ldots,N$ indicates the layer number. The latter index is present only if $m = A, B$, see Fig. 1. The real amplitude of the electric component of the linearly polarized electromagnetic field in subspace mn reads in a Fourier representation as

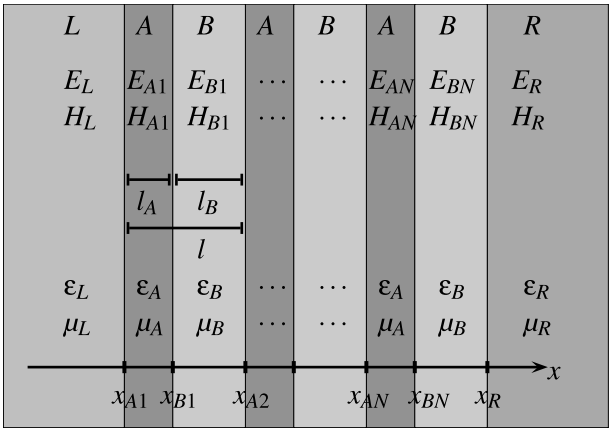

Fig. 1. The stratified one-dimensional N-layer medium and its surroundings. Slabs A and B, which, respectively have physical widths l_A and l_B, together form a single layer of thickness l. Along the principal axis, the x-axis, the interface coordinates have been written. The permittivities and permeabilities of material $m = L,A, B, R$ are, respectively given by ϵ_m and μ_m. Also indicated is the labeling of the electric (E) and magnetic (H) field amplitudes in the various homogeneous subspaces of the system.

$$E_{mn}(t,x) = \int \mathrm{d}\omega \widetilde{E}_{mn}(\omega;x) \exp(-\mathrm{i}\omega t). \tag{3}$$

where the complex Fourier coefficient is given by

$$\widetilde{E}_{mn}(\omega;x) = \frac{1}{2\pi} \int \mathrm{d}t E_{mn}(t,x) \exp(\mathrm{i}\omega t). \tag{4}$$

These coefficients obey Helmholtz' equation,

$$(\partial_x^2 + k_m^2)\widetilde{E}_{mn}(\omega;x) = 0, \tag{5}$$

where

$$k_m = \omega\sqrt{\epsilon_m \mu_m}. \tag{6}$$

The solutions to Eq. (5) give, after substitution into Eq. (3), that the electric field consists of, respectively the right- and leftwards propagating parts

$$E_{mn}^{(r)}(t,x) = \int \mathrm{d}\omega \widetilde{E}_{mn}^{(r)}(\omega) \exp(-\mathrm{i}\omega t + \mathrm{i}k_m(x - x_{mn})), \tag{7a}$$

$$E_{mn}^{(l)}(t,x) = \int \mathrm{d}\omega \widetilde{E}_{mn}^{(l)}(\omega) \exp(-\mathrm{i}\omega t - \mathrm{i}k_m(x - x_{mn})), \tag{7b}$$

where the Fourier coefficients of respectively the right- and leftwards propagating parts of the electric field, as evaluated at the interfaces, are given by

$$\widetilde{E}_{mn}^{(r)}(\omega) = \frac{1}{2\pi} \int \mathrm{d}t E_{mn}^{(r)}(t, x_{mn}) \exp(\mathrm{i}\omega t), \tag{8a}$$

$$\widetilde{E}_{mn}^{(l)}(\omega) = \frac{1}{2\pi} \int \mathrm{d}t E_{mn}^{(l)}(t, x_{mn}) \exp(\mathrm{i}\omega t). \tag{8b}$$

From Maxwell's equation $\nabla \times \widetilde{\mathbf{E}} - \mathrm{i}\omega\widetilde{\mathbf{B}} = 0$ with $\widetilde{\mathbf{B}} = \mu\widetilde{\mathbf{H}}$, the Fourier coefficients of, respectively the right- and leftwards propagating parts of the magnetic field that correspond to those of the electric fields of Eq. (8a) follow as

$$\widetilde{H}_{mn}^{(r)} = -\widetilde{E}_{mn}^{(r)}/Z_m, \tag{9a}$$

$$\widetilde{H}_{mn}^{(l)} = \widetilde{E}_{mn}^{(l)}/Z_m, \tag{9b}$$

[1] For the evolution of precursors in homogeneous media with multiple electron resonances, see Ref. [14].

where $Z_m = \sqrt{\mu_m/\epsilon_m}$ is the impedance of material m. The left-to-right transmission coefficient of the photonic crystal for the electric field amplitude is defined as

$$t_N \equiv (\widetilde{E}_{\mathrm{R}}^{(r)}/\widetilde{E}_{\mathrm{L}}^{(r)})|_{\widetilde{E}_{\mathrm{R}}^{(l)}=0}, \tag{10}$$

and in the rest of this section we will calculate t_N. Let $x_{m'n'}$ denote the coordinate of the interface immediately to the right of the interface at $x = x_{mn}$. The electric and magnetic fields must be continuous at each interface, hence

$$E_{mn}(t, x_{m'n'}) = E_{m'n'}(t, x_{m'n'}), \tag{11a}$$
$$H_{mn}(t, x_{m'n'}) = H_{m'n'}(t, x_{m'n'}). \tag{11b}$$

With Eqs. (3), (8a) and (9b), (11a) give

$$\begin{pmatrix} \widetilde{E}_{m'n'}^{(r)} \\ \widetilde{E}_{m'n'}^{(l)} \end{pmatrix} = \Theta_{m'm} \Pi_m \begin{pmatrix} \widetilde{E}_{mn}^{(r)} \\ \widetilde{E}_{mn}^{(l)} \end{pmatrix}, \tag{12}$$

where the transmission matrix $\Theta_{m'm}$ is constructed from the dynamical matrices

$$\Delta_m = \begin{pmatrix} 1 & 1 \\ -Z_m^{-1} & Z_m^{-1} \end{pmatrix} \tag{13}$$

as

$$\Theta_{m'm} = \Delta_{m'}^{-1} \Delta_m. \tag{14}$$

Note that by construction $\Theta_{m'm}^{-1} = \Theta_{mm'}$ and $\Theta_{m'm}\Theta_{mm''} = \Theta_{m'm''}$. Further, in Eq. (12), the unimodular propagation matrices are given by

$$\Pi_m = \mathrm{diag}(\exp(\mathrm{i}k_m l_m), \exp(-\mathrm{i}k_m l_m)). \tag{15}$$

Eq. (12) relates the Fourier coefficients of the left- and rightwards propagating electric field components in subsequent slabs. The single-layer transfer matrix involves transfer over two successive slabs,

$$T_A = \Theta_{AB} \Pi_B \Theta_{BA} \Pi_A. \tag{16}$$

The entries of $T_A = \begin{pmatrix} A_1 & B_1 \\ C_1 & D_1 \end{pmatrix}$ can readily be calculated as

$$A_1 = \exp(\mathrm{i}k_A l_A)\left(\cos k_B l_B + \frac{\mathrm{i}}{2}\left(\frac{Z_A}{Z_B} + \frac{Z_B}{Z_A}\right)\sin k_B l_B\right), \tag{17a}$$
$$B_1 = \frac{\mathrm{i}}{2}\exp(-\mathrm{i}k_A l_A)\left(\frac{Z_B}{Z_A} - \frac{Z_A}{Z_B}\right)\sin k_B l_B, \tag{17b}$$
$$C_1 = \frac{-\mathrm{i}}{2}\exp(\mathrm{i}k_A l_A)\left(\frac{Z_B}{Z_A} - \frac{Z_A}{Z_B}\right)\sin k_B l_B, \tag{17c}$$
$$D_1 = \exp(-\mathrm{i}k_A l_A)\left(\cos k_B l_B - \frac{\mathrm{i}}{2}\left(\frac{Z_A}{Z_B} + \frac{Z_B}{Z_A}\right)\sin k_B l_B\right). \tag{17d}$$

With a slight simplification by using the aforementioned properties of Θ_{mn}, the left-to-right transfer matrix of the N-layer medium, T, can be constructed from the propagation and transmission matrices as

$$T = \Theta_{\mathrm{RA}} T_A^N \Theta_{\mathrm{AL}}. \tag{18}$$

Note that $\det T = Z_{\mathrm{R}}/Z_{\mathrm{L}}$. The unimodularity of T_A implies that the entries of the transfer matrix for N layers,

$$T_A^N \equiv \begin{pmatrix} A_N & B_N \\ C_N & D_N \end{pmatrix}, \tag{19}$$

are related to those of the single-layer transfer matrix as [16]

$$A_N = A_1 U_{N-1}(T_1) - U_{N-2}(T_1), \tag{20a}$$
$$B_N = B_1 U_{N-1}(T_1), \tag{20b}$$
$$C_N = C_1 U_{N-1}(T_1), \tag{20c}$$
$$D_N = D_1 U_{N-1}(T_1) - U_{N-2}(T_1), \tag{20d}$$

where the U_m are the Chebyshev U-polynomials,

$$U_m(T_1) = \sum_{n=0}^{\lfloor \frac{m}{2} \rfloor} (-1)^n \binom{m-n}{n} (2T_1)^{m-2n}, \tag{21}$$

having as argument $T_1 \equiv \frac{1}{2}\mathrm{tr}T_A$. In Eq. (21) the upper limit to the sum, $\lfloor \frac{m}{2} \rfloor$, denotes the floor function of $m/2$, which gives the largest integer that is smaller than or equal to $m/2$. From the defining equation of the transfer matrix,

$$\begin{pmatrix} \widetilde{E}_{\mathrm{R}}^{(r)} \\ \widetilde{E}_{\mathrm{R}}^{(l)} \end{pmatrix} = \begin{pmatrix} T_{11} & T_{12} \\ T_{21} & T_{22} \end{pmatrix} \begin{pmatrix} \widetilde{E}_{\mathrm{L}}^{(r)} \\ \widetilde{E}_{\mathrm{L}}^{(l)} \end{pmatrix}, \tag{22}$$

the N-layer medium's left-to-right[2] transmission coefficient for the electric field follows from Eq. (10) in terms of the T-matrix entries as

$$t_N = \frac{\det T}{T_{22}}. \tag{23}$$

This expression gives the transmission of the N-layer medium in frequency space and the left-to-right transmitted electric field amplitude, evaluated at the exit plane of the N-layer medium, follows from Eqs. (7a) and (10) in terms of the applied field spectrum and the transmission coefficient as

$$E_{\mathrm{R}}^{(r)}(t) = \int \mathrm{d}\omega t_N(\omega) \widetilde{E}_{\mathrm{L}}^{(r)}(\omega) \exp(-\mathrm{i}\omega t). \tag{24}$$

In the following section we will consider the transmittance for complex frequencies in order to determine, as a function of time, those frequency components that are transmitted with the least absorption. This will be done for early times, so that we obtain, by using the method of steepest descent, the time-resolved, initial transmitted frequency components.

4. Transmittance of the photonic crystal

In anticipation of the application of the method of steepest descent, we write the propagation part of the integrand of Eq. (24) as a mono-exponential function and we use the natural time coordinate for the N-layer system, $\Theta_N = ct/(Nl)$. With these substitutions, the transmitted field reads as

$$E_{\mathrm{R}}(\Theta_N) = \int \mathrm{d}\omega \widetilde{E}_{\mathrm{L}}(\omega) \exp \Phi_N(\Theta_N; \omega). \tag{25}$$

We have omitted the superscript to indicate that the field propagates rightwards, since from now on we will only consider rightwards propagating fields. The exponent that describes the propagation is called the (complex) phase function [17] and it is given by

$$\Phi_N = \ln t_N - \mathrm{i}\omega(Nl/c)\Theta_N. \tag{26}$$

The transmittance of the medium is by definition the ratio of the transmitted field intensity to the applied field intensity and it follows from Eqs. (25) and (27) as $T_N = \exp(2\ \mathrm{Re}\,\Phi_N)$. Note that the transmittance is independent of the shape of the applied pulse, it is a function of the system parameters. A plot of

$$X_N = \mathrm{Re}\Phi_N, \tag{27}$$

in the complex plane is therefore a scaled, logarithmic plot of the transmittance for complex frequencies. Fig. 2 shows various of these plots, successive plots being taken at successive instants of time. The coordinates along the axes are given by $\xi = \mathrm{Re}\,\omega$ and $\eta = \mathrm{Im}\,\omega$. The values that were used for the medium parameters have been listed in Table 1. The value of X_N is constant on contour lines and this value has been indicated for two neighboring contour lines in each plot. The difference of the values of X_N on neighboring contour lines is constant as well. Reality of the

[2] The right-to-left transmission coefficient equals $t'_N \equiv .(\widetilde{E}_{\mathrm{L}}^{(l)}/\widetilde{E}_{\mathrm{R}}^{(l)})|_{\widetilde{E}_{\mathrm{L}}^{(r)}=0} = T_{22}^{-1}$, the two transmission coefficients are therefore related as $Z_R t'_N = Z_L t_N$.

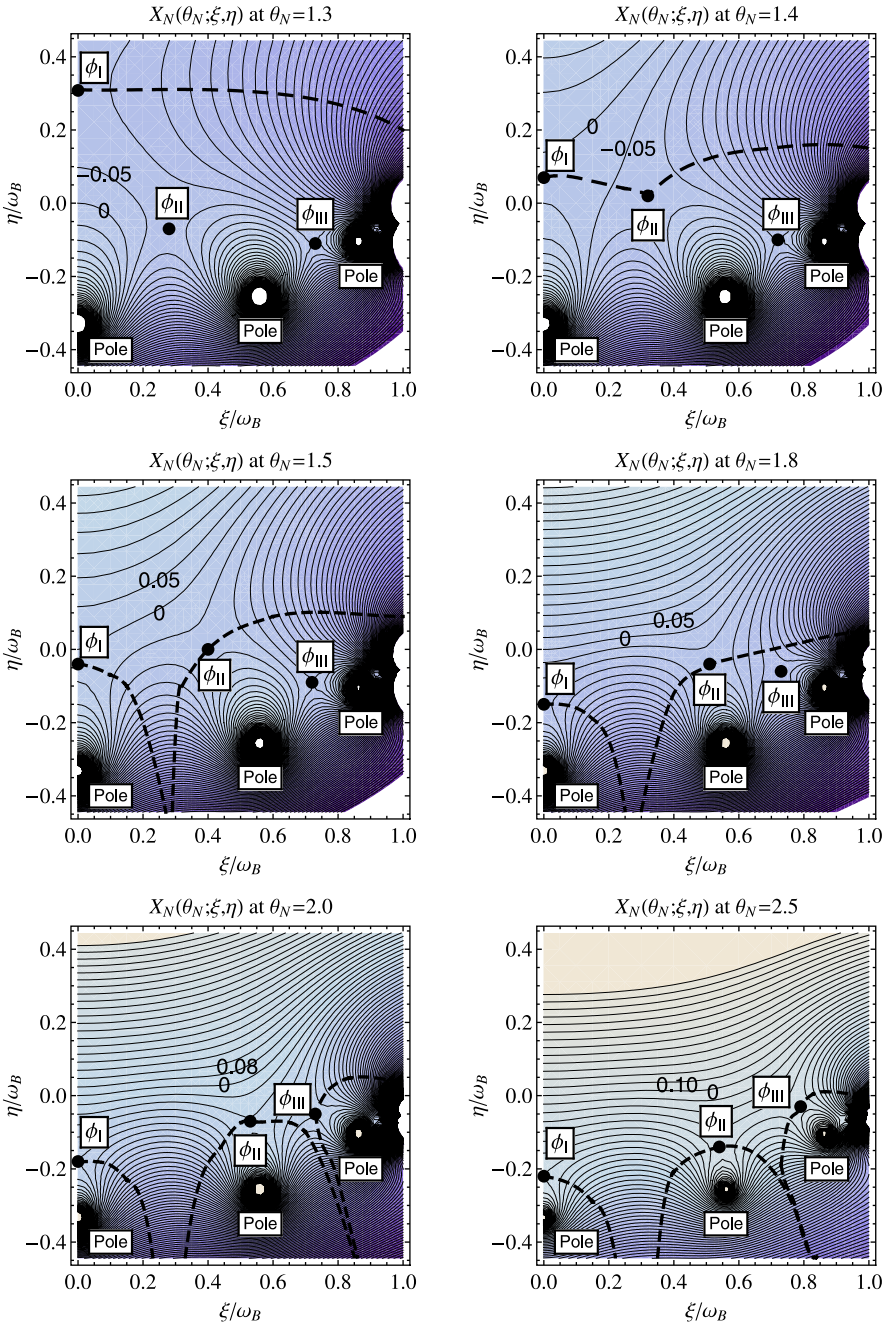

Fig. 2. Plots of X_N, which is one half times the logarithm of the transmittance of the N-layer medium, at increasing values of time θ_N for $N = 1$ and the parameter values of Table 1. The value of X_N is constant on contour lines and the difference of neighboring contour values is constant in each plot. The two numbers in each plot give contour values. The dashed curve represents the integration path, along which the stationary points have been indicated.

field amplitudes implies that $\Phi_N^*(\omega) = \Phi_N(-\omega^*)$ which in turn implies that X_N is symmetric about the imaginary axis, therefore the plots cover only positive values of ξ. The lowest electron resonance frequency ω_B sets the upper limit for the frequencies of the Brillouin precursor, therefore the frequency domains of the plots have been chosen to extend until this frequency and the coordinates ξ and η are measured in units of this frequency. The plotting times have been chosen such that they cover the time interval during which those stationary points of the phase function that generate the Brillouin precursor are dominant as compared to all other stationary points of the phase function throughout the complex plane. With dominant stationary points we mean those stationary points at which X_N takes on the largest values. In the plots of Fig. 2, the stationary points of the phase function appear as saddle-points, see Appendix A. At the plotting times, all stationary points in the plots are of first order, as can

Table 1
Parameter values that have been used for the transmittance plots

Medium parameter values		
Number of layers	$N = 1$	
Slab widths[a]	$l_A = 20$ nm	$l_B = 30$ nm
Electron resonances	$\omega_A = 4.0 \times 10^{16}$/s	$\omega_B = 2.5 \times 10^{16}$/s
Plasma frequencies	$\omega_{pA} = 4.5 \times 10^{16}$/s	$\omega_{pB} = 2.0 \times 10^{16}$/s
Absorption parameters	$\gamma_A = 0.20 \times 10^{16}$/s	$\gamma_B = 0.15 \times 10^{16}$/s
Permittivities surrounding media	$\epsilon_L = \epsilon_0$	$\epsilon_R = \epsilon_0$

[a] The reason for taking the slab widths so small is given in the discussion.

be concluded from the variation of X_N in the neighborhood of these points. Figs. 3 and 4

5. Method of steepest descent

The three dominant stationary points in Fig. 2 have been indicated and, following the method of steepest descent, the instantaneous integration path passes through these stationary points, it is given by the dashed curve. Away from the stationary points, this path follows the lines of steepest descent of X_N. The contribution to the electric field of Eq. (25) that comes from the integration in the neighborhood of a first-order stationary point of the phase function that follows the trajectory $\omega = \phi_s\ (\theta_N)$ is given, within the approximation of the method of steepest descent, by

$$E_R^{(s)}(\theta_N) = \widetilde{E}_L(\phi_s)\Pi(\theta_N, \phi_s), \tag{28}$$

where we have defined the function that describes, within this approximation, the effects of the propagation in the medium on the transmitted field as

$$\Pi(\theta_N; \phi_s) = \sqrt{2\pi}\left|\Phi_N^{(2)}(\phi_s)\right|^{-\frac{1}{2}} \exp(\Phi_N(\theta_N; \phi_s) + i\alpha_N(\phi_s)), \tag{29}$$

where $\Phi_N^{(n)}$ denotes the n-th order ω-derivative of the phase function and where $\alpha_N(\phi_s) = (\pi/2) - (1/2)\arg\Phi_N^{(2)}(\phi_s)$ is the angle of the steepest descent line with the positive real axis at the stationary point. The integration in Eq. (25) in the neighborhood of the stationary point has been performed in the direction of this steepest descent line. Eq. (28) only holds if the phase function is stationary to first order along the trajectory. In order to determine the roots of the second-order derivative of the phase function for verifying that these are not located on the trajectory and thus represent second-order stationary points, the function

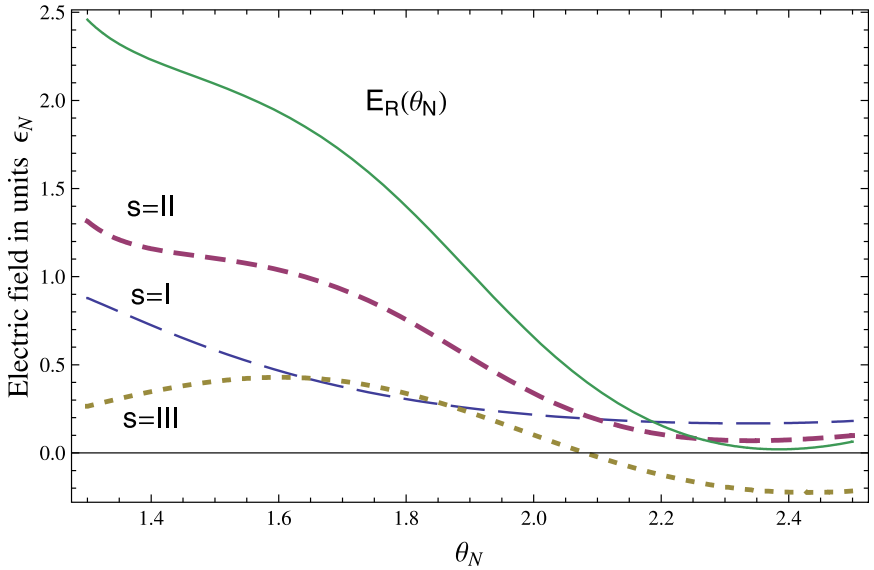

Fig. 3. Calculated electric field amplitude (solid line) as a function of time, resulting from an applied delta-peak input pulse, after transmission through the layered medium with $N = 1$. The dashed lines give twice the real part of the contributions from the three dominant stationary points.

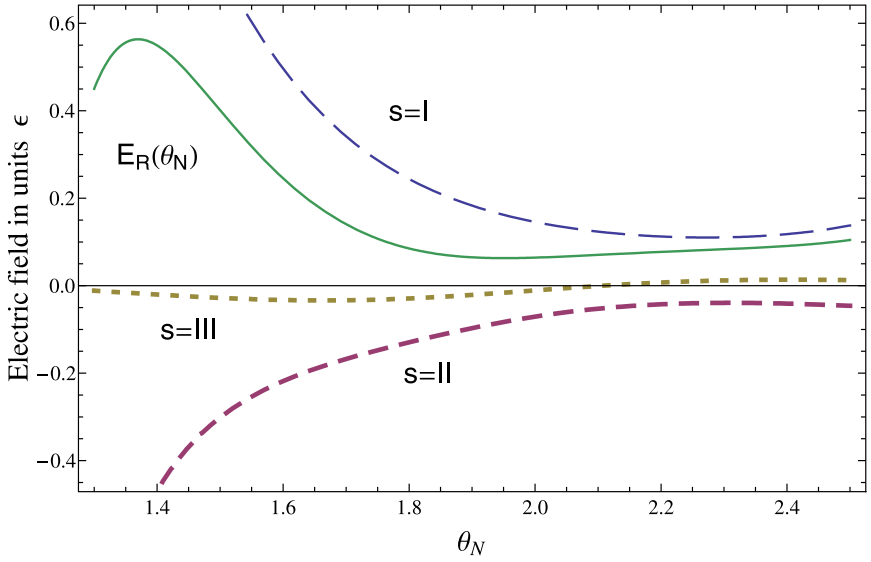

Fig. 4. Calculated electric field amplitude (solid line) as a function of time, resulting from an applied Heaviside step-modulated input pulse, after transmission through the layered medium with $N = 1$. The dashed lines give twice the real part of the individual contributions from the three dominant stationary points.

$$U_N = \mathrm{Re}\Phi_N^{(1)} \tag{30}$$

has been plotted in Fig. 5, again for the parameter values of Table 1. In this figure, the roots of the second-order derivative of the phase function are visible as saddle-points. From Eq. (26), it follows that U_N is independent of time, so the positions of the roots of the second-order derivative of the phase function are fixed. The roots of first- and second-order derivative of the phase function, as determined from, respectively Figs. 2 and 5, have been plotted together in Fig. 6. In this figure, the dashed lines connect successive instantaneous stationary points of the phase function and thus roughly represent the observed trajectories. From this figure, it follows that the stationary points are always of first order at the time interval spanned by the plots in Fig. 2, because the roots of first- and second-order derivatives of the phase function do not coincide in this time interval. Therefore, we are allowed to use Eq. (28) for a calculation of the transmitted field.

We will now obtain an algebraic expression for the stationary point trajectory $\omega = \phi_s(\theta_N)$, which is required for Eq. (28). When at some observation time $\theta_N = \theta_s$ the instantaneous location of a stationary point of the phase function is determined from the transmittance plots as $\omega = \omega_s$, its trajectory at times close to this evaluation time follows from the relation $\Phi_N^{(1)} = 0$ together with the requirement that $\phi_s(\theta_s) = \omega_s$ and is given by [18,19]

$$\phi_s(\theta_N) = \omega_s + \sum_{l=1}^{\infty} \frac{(-1)^l}{l!} \left[\partial_{\widetilde{\omega}}^{l-1} \left(\widetilde{\Phi}_N(\widetilde{\theta}_N; \widetilde{\omega}) - \widetilde{\omega} \right)^l \right]_{|\left(\widetilde{\theta}_N, \widetilde{\omega}\right)}, \tag{31}$$

Here, the auxiliary function $\widetilde{\Phi}_N(\widetilde{\theta}_N; \widetilde{\omega}) = \Phi_N^{(1)}(\widetilde{\theta}_N + \theta_s; \widetilde{\omega} + \omega_s)/\Phi_N^{(2)}(\theta_s; \omega_s)$ that picks out the proper stationary point, is well-defined if the observed stationary point is of first order. For the plots of Fig. 2, this requirement is fulfilled because we have already verified that the stationary points are of first order along the complete trajectory. The trajectories as calculated from Eq. (31) are shown in Fig. 6 as solid lines. These do diverge a little from the observed trajectories at times that differ much from the observation time, which is at $\theta_s = 1.8$, and which has been used as the origin in the function series expansion of Eq. (31). This stems from the fact that the sum in Eq. (31) could only be taken up to and including the third term because of a shortage of computer power.

At last, we mention that the aforementioned symmetry of the phase function implies that, if it has a stationary point at $\omega = \phi_s$, it also has one at $\omega = -\phi_s^{\star}$. When an integration path is used that is symmetric about the imaginary axis, as we will do because X_N is symmetric about his axis, the contribution from the one stationary point equals the complex conjugate of the contribution from the other so that both together give a real field with an amplitude that equals twice the real part of Eq. (28). This completes the discussion about how to obtain the dominant contributions to the transmitted field from a temporal sequence of graphs of the transmittance and the method of steepest descent. In the next section, the electric field contributions from the dominant stationary points will be numerically calculated for two applied fields: the delta-peak pulse and a step-modulated sinusoidally oscillating field.

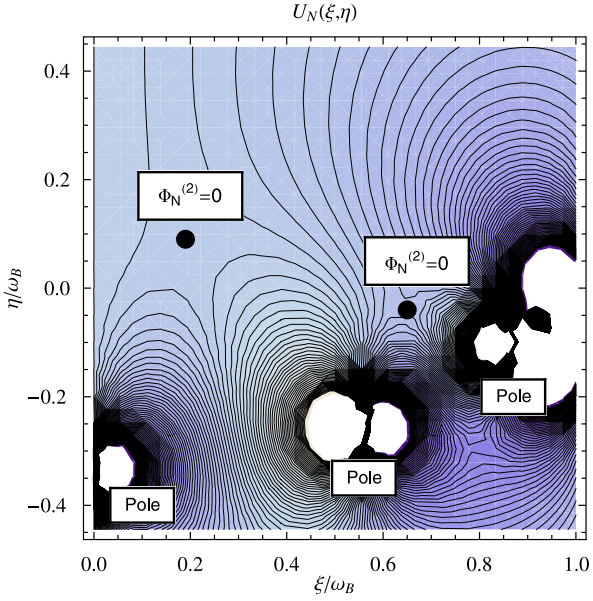

Fig. 5. Plot of $U_N = \mathrm{Re}\,\Phi_N^{(1)}$. The roots of $\Phi_N^{(2)} = 0$ are visible as saddle-points of U_N.

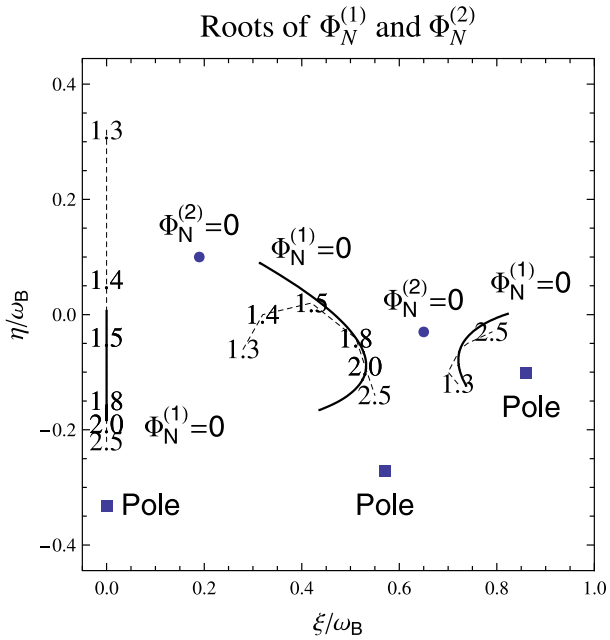

Fig. 6. The time-dependent roots of $\Phi_N^{(1)}$ and the time-independent roots of $\Phi_N^{(2)}$ as obtained from, respectively the contour plots of X_N and U_N. The numbers denote the values of time θ_N and give the instantaneous locations of the roots of $\Phi_N^{(1)}$. The solid lines represent the stationary point trajectories $\omega = \phi_I(\theta_N)$ (leftmost solid line), $\phi_{II}(\theta_N)$ (middle) and $\phi_{III}(\theta_N)$ (right) in the time interval $1.3 \leqslant \theta \leqslant 2.5$, as calculated from the series expansion formula about evaluation time $\theta_s = 1.8$.

6. Results

The Brillouin precursor arises predominantly as a result of the specific dispersion and absorption of the medium and it is quite independent of the actual shape of the applied pulse [1]. Because our main interest is in the effect of the inhomogeneities of the medium on this precursor, we will only consider two simple input pulses, namely a delta-peak and a step-function modulated sinusoidal oscillation. For the delta-pulse, the applied field is given by $E_L(t) = \epsilon\delta(t)$ where ϵ is the strength of the pulse. In natural time units, this applied field reads as

$$E_L(\theta_N) = \epsilon_N \delta(\theta_N), \tag{32}$$

where $\epsilon_N = (Nl)^{-1} c\epsilon$ is a strength with the dimension of an electric field amplitude. For the input pulse of Eqs. (32), (28) gives that the contribution to the transmitted field from a stationary point at $\omega = \phi_s(\theta_N)$ equals

$$E_R^{(s)}(\theta_N) = \frac{Nl\epsilon_N}{2\pi c} \Pi(\theta_N; \phi_s). \tag{33}$$

Since the propagation part Π in this expression is merely multiplied with a constant coefficient, the transmitted field that results from an

applied delta-peak input pulse most clearly exhibits the effects of the medium. The field of Eq. (33) has been plotted in Fig. 6 for the three dominant stationary points to which we have added the contributions from the corresponding stationary points at the opposite side of the imaginary axis. Shown are the individual contributions from the stationary points and their sum, which approximately makes up for to the total transmitted field at the plotted time interval.

In order to be able to compare the amplitude of the transmitted Brillouin precursor to that of an applied pulse, which is difficult to do for the delta-peak input pulse, we also consider the Heaviside step-function modulated input signal

$$E_{\mathrm{L}}(t) = \epsilon\theta(t)\sin\omega_0 t, \tag{34}$$

where ϵ is the amplitude and ω_0 the angular frequency of the field at times greater than zero and $\theta(t)$ is the unit step function. For this input field, Eq. (28) gives the contribution from a stationary point at $\omega = \phi_{\mathrm{s}}$ to the transmitted field as

$$E_{\mathrm{R}}^{(\mathrm{s})}(\theta_N) = \frac{\epsilon}{2\pi}\frac{\omega_0}{\omega_0^2 - \phi_{\mathrm{s}}^2}\Pi(\theta_N;\phi_{\mathrm{s}}). \tag{35}$$

This field has been plotted in Fig. 6, for which we have used as carrier frequency $\omega_0 = 4\times10^{15}\ \mathrm{s}^{-1}$. The amplitude is given in units ϵ and for the Brillouin precursor it is maximally about 0.6 times that of the applied field. The amplitudes of applied and transmitted field are still comparable because, for the choice of parameters $N = 1$, $l_A = 20$ nm and $l_{\mathrm{B}} = 30$ nm, the propagation distance in the medium is only 50 nm and over such a short distance the absorption is very small. Below, in the discussion section, we will give our reasons for taking such a small propagation distance.

7. Discussion

From Eq. (29) it follows that the instantaneous frequency of the contribution from a stationary point is approximately equal to its horizontal coordinate if this point moves slowly in time. This is especially the case at late times $\theta_N \gtrsim 2$, when the motion of the stationary points comes to rest, close to the scattering resonance poles (see Fig. 2). Hence, at late times, the transmittance spectrum peaks at the resonance frequencies, whereas the Bragg-scattering frequency components that lie in between the resonance poles, are slightly suppressed. In Fig. 6, it is visible that the field from $\omega = \phi_I$ is an exponentially decaying non-oscillating field, whereas the other contributions are not only decaying, but also oscillating fields.

Our observation from Fig. 2 is that the number of stationary points of the phase function and their locations in the complex plane are strongly tied up with the number of singularities of this function and their locations, however we cannot quantify this statement. Therefore, we will now discuss the density and location of the singularities of the phase function and argue how these affect the transmitted field. As can be seen in Fig. 2, the locations of the singularities of Φ_N in the complex plane are independent of time. The singularities originate from two possible causes. The slab permittivities ϵ_A and ϵ_B each have two poles in the complex plane. From Eq. (2b), their locations are given by

$$\omega = \pm\sqrt{\omega_m^2 - \gamma_m^2} + \mathrm{i}\gamma_m, \quad m = A, B. \tag{36}$$

The permittivities of media L and R have no poles since these media were chosen as vacuum. The poles of the permittivities always appear as branch-points of X_N since it is always the square root of the permittivity that enters the expressions of the transmitted field, see Eqs. (17d). The branch points of Eq. (36) for $m = A$ are located outside of the domain of the plots of Fig. 2 whereas for $m = B$ one is situated at $\omega \simeq (1 - 0.06\mathrm{i})\omega_B$. The locations of the permittivity poles of Eq. (36) are independent of the geometry of the medium, which is governed by the parameters N and l_A and l_{B}.

The other singularities are the geometric resonance frequencies which emerge in the landscape of X_N as poles. These poles are the roots of T_{22} (the 2,2-element of the transfer matrix, see Eq. (23)) and they are visible in Fig. 2 as white dots. In the figure, it is visible that the poles cluster at the branch-point of slab B. This is explained as follows. The wavelength of the field in medium m is given by

$$\lambda_m = \frac{2\pi}{\mathrm{Re}k_m}. \tag{37}$$

For frequencies close to the branch-point of this medium, the wavelength becomes very small and as a consequence, many wavelengths fit in the slab giving many resonance poles, thus explaining the clustering. The density of the geometric resonance poles increases with the number of layers N and with the slab widths l_A and l_B since more wavelengths fit in the system when the medium is made larger. The values of these parameters were chosen small in order to keep the number of stationary points that give significant contributions to the Brillouin precursor small: we only had to take into account three stationary point contributions.

There is also a serious drawback of taking the dimensions of the medium small. As mentioned earlier, for our choice of parameters the medium width is only 50 nm. The phase function, and therewith X_N, scales with these parameters. In the case of propagation in a homogeneous medium, the propagation distance is a linear overall scaling parameter of the exponent of the phase function. For an inhomogeneous medium, the number of layers and the slab widths are not simple linear overall scaling parameters, though the variation of X_N does become small when the dimensions of the medium are taken to be small. In the extreme case $N = 0$, $l_A = 0$ and $l_B = 0$ there is no variation at all since then $X_N \equiv 0$ everywhere. The small variation of X_N in the complex plane is visible in Fig. 2 as the small difference of the values of X_N on neighboring contour lines, which is about 0.05. For larger medium dimensions, the variation in X_N becomes larger and the stationary point contributions are more pronounced. This latter situation reflects the mature regime [14] of the dispersion, in which the shape of the field has fully developed to a steady pattern. So, for our choice of parameters, the transmitted field has not yet fully reached the steady state.

Fig. 7 is an instantaneous plot of X_N for the same set of parameter values as that has been used for Fig. 2, except for the number of layers, which is now taken equal to $N = 5$. This figure shows three consequences of increasing the number of layers. At first, the density of scattering resonance poles increases, which has been explained above. Secondly, the resonance poles have been shifted towards the real axis. The vertical position of a pole in the complex plane is related to the contrast of the complete medium at the frequency of the pole. This can easily be shown for a slab of width l_A and of constant, real, refractive index n_A. The Fresnel reflection and Fresnel transmission coefficients for the interfaces of the slab are, respectively r_{AB} and t_{AB}. Then the transmission coefficient of this slab equals $t_{slab} = t_{AB}t_{BA}\exp(\mathrm{i}l_A n_A\omega/c)/(1 - r_{AB}^2\exp(2\mathrm{i}l_A n_A\omega/c))$. The relation for resonance is $r_{AB}^2\exp(\mathrm{i}l_A n_A\omega/c) = 1$, therefore the vertical coordinate of the pole follows as $\eta = \frac{c}{l_A n_A}\log|r_{AB}|$. Since $0 < |r_{AB}| < 1$, the pole lies below the real axis and approaches this axis if the contrast $|r_{AB}|$ approaches its maximum value of one. When the number of layers increases, the overall medium contrast increases as well and therefore the poles are shifted towards the real axis. At last, the transmittance minimum at the band-gap becomes visible. It is located between the N-th and the $N+1$-th resonance poles with nonzero frequency, at $\omega \simeq (0.57 - 0.05\mathrm{i})\omega_B$.

At last, the Brillouin precursor that arises in our inhomogeneous N-layer medium that consists of homogeneous slabs with each one

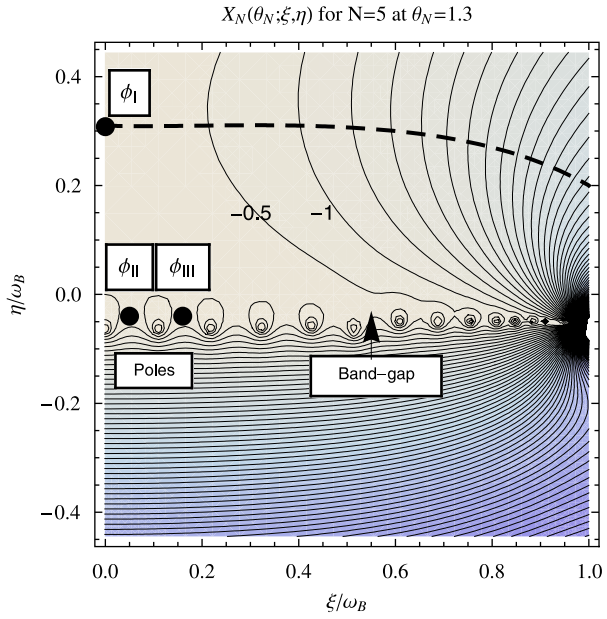

Fig. 7. Plot of contours of X_N for $N = 5$ and again for the parameter values listed in Table 1. The main differences with the previous plots for $N = 1$ are explained in the text.

electron resonance is compared with the Brillouin precursor that arises in a homogeneous medium with two electron resonances [14]. For comparison, the two slab electron resonances of the inhomogeneous medium are taken to be equal to the electron resonances of the homogeneous medium. In the case of the multiple-layer medium, we have found that the Brillouin precursor is generated from the frequency components below the lowest electron resonance frequency of the two slabs and the forerunner is slightly distorted such that the (geometric) resonant frequency components are enhanced and the Bragg-scattered frequency components are suppressed, as has been concluded from the transmittance landscape. In the case of the double-resonance homogeneous medium, the Brillouin precursor is generated from the same low-frequency components, but the distortion is absent.

8. Conclusions

We have investigated the electromagnetic Brillouin precursor that has been transmitted through a one-dimensional photonic crystal, modeled by the stratified layered medium. This precursor is formed by those components of the applied pulse that have frequencies smaller than the lowest electron resonance frequency of the medium. From an investigation of the transmittance and from applying the method of steepest descent, the following observations have been made. The effect of the slab contrast on the spectrum of the transmitted Brillouin precursor is that, after a certain rise time, the components with frequencies equal to the frequencies of the poles of the transmission coefficient are slightly enhanced and the Bragg-scattering frequency components that lie in between the poles, are suppressed.

Acknowledgements

The authors thank Prof. J. Knoester for his useful suggestions. This research is supported by NanoNed, a national nanotechnology programme coordinated by the Dutch Ministry of Economic Affairs.

Appendix A. Steepest descent method

In order to illustrate the method of steepest descent, we use the integral of Eq. 25,

$$E_R(\theta) = \int d\omega \widetilde{E}_L(\omega) \exp \Phi(\theta;\omega), \tag{38}$$

where we have omitted the various N-subscripts and (r)-superscripts, as we will do throughout this appendix. We assume that $\widetilde{E}_L$ varies slowly as a function of ω as compared to Φ in the neighborhood of the relevant stationary points of the latter function. Let X and Y, respectively denote the real and imaginary parts of Φ and let ξ and η denote, respectively the real and imaginary parts of ω. Demanding $\Phi^{(1)}$, which denotes the first-order ω-derivative of Φ, to be independent of the direction along which the derivative is taken in the complex plane gives the Cauchy-Riemann equations,

$$X_\xi = Y_\eta, \quad X_\eta = -Y_\xi, \tag{39}$$

where $X_\xi = \partial X/\partial\xi$ etcetera. Let τ parametrize the deformed integration path. When this path follows the steepest slope lines of X, the coordinate derivative must satisfy

$$\begin{pmatrix} \dot{\xi} \\ \dot{\eta} \end{pmatrix} = \pm \begin{pmatrix} X_\xi \\ X_\eta \end{pmatrix}, \tag{40}$$

where the dot denotes the τ-derivative and where the plus and minus sign stand for, respectively the steepest ascent and descent lines. From the chain rule for differentiation and from Eqs. (39) and (40) it follows that

$$\dot{Y} = 0. \tag{41}$$

This proves that the phase is constant along the lines of steepest descent. The n-th order stationary points of Φ satisfy

$$\Phi^{(k)} = 0, \quad k = 1,\ldots,n. \tag{42}$$

When Φ depends on time θ as well, the stationary points generally sweep out trajectories in ω-space and we write the solutions to Eq. (42) as

$$\omega = \phi_s(\theta). \tag{43}$$

The Taylor expansion of Φ in ω about an n-th order stationary point at $\omega = \phi_s(\theta)$ is equal to

$$\Phi(\theta;\omega) = \Phi(\theta;\phi_s(\theta)) + \frac{\Phi^{(n+1)}(\theta;\phi_s(\theta))}{(n+1)!}(\omega-\phi_s(\theta))^{n+1} + o((\omega-\phi_s(\theta))^{n+2}). \tag{44}$$

With polar coordinates in the complex ω-plane it easily follows that, at an n-th order stationary point of Φ, both X and Y have a saddle-point from which $n + 1$ radial lines of steepest descent and as-

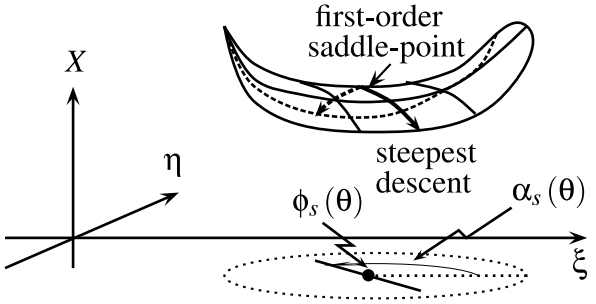

Fig. 8. Illustration of an instantaneous plot of $X(\theta;\xi,\eta) = \mathrm{Re}\ \Phi(\theta;\omega)$ near a first-order stationary point of Φ at $\omega = \phi_s$. The steepest descent lines depart from this point along the radial line at the angle $\alpha = \alpha_s$ and in the opposite direction.

cent depart. For first-order stationary points, the contribution to the field can actually be calculated and Fig. 8 illustrates X at a fixed time θ close to a first-order stationary point at $\omega = \phi_s(\theta)$. The angles of the steepest descent lines of X departing from this point are given by

$$\alpha_s(\theta) = \frac{1}{2}(\pi - \arg \Phi^{(2)}(\theta; \phi_s(\theta))), \tag{45}$$

and the other is at $\alpha_s + \pi$. When the integration path is taken along the radial line at angle α_s through this point, the parametrization of the path equals $\omega = \phi_s(\theta) + e^{i\alpha_s(\theta)}\tau$ and the contribution from this stationary point to the field of Eq. (38) can be calculated with a quadratic approximation of Φ as

$$\begin{aligned} E_R^{(s)}(\theta) &= \widetilde{E}_L(\phi_s)\exp(\Phi(\theta;\phi_s) + i\alpha_s)\int d\tau \exp\left(-\tfrac{1}{2}|\Phi^{(2)}(\theta;\phi_s)|\tau^2\right), \\ &= \sqrt{2\pi}\widetilde{E}_L(\phi_s)\exp(\Phi(\theta;\phi_s) + i\alpha_s)|\Phi^{(2)}(\theta;\phi_s)|^{-\frac{1}{2}}. \end{aligned} \tag{46}$$

The symmetry $\Phi_N^*(\theta_N, \omega) = \Phi_N(\theta_N, -\omega^*)$ implies that, if Φ has a stationary point at $\omega = \phi_s$, it also has one at $\omega = -\phi_s^{\star}$. When an integration path is used that is symmetric about the imaginary axis, the contribution from one stationary point equals the complex conjugate of the other so that both stationary points together contribute two times the real part of Eq. (46).

References

[1] A. Sommerfeld, L. Brillouin, Ann. der Physik 4 (10) (1914) 177.
[2] P. Pleshko, I. Palócz, Phys. Rev. Lett. 22 (1969) 1201.
[3] J.D. Joannopoulos, R.D. Meade, J.N. Winn, Photonic Crystals, Molding the Flow of Light, Princeton University Press, 1995.
[4] S. Zhu, N. Liu, H. Zheng, H. Chen, Opt. Commun. 174 (2000) 139.
[5] P.W. Milonni, J. Phys. B 35 (2002) R31.
[6] J.N. Munday, M. Robertson, Appl. Phys. Lett. 83 (2003) 1053.
[7] M. Scalora, J.P. Dowling, M.J. Bloemer, C.M. Bowden, J. Appl. Phys. 76 (1994) 2023.
[8] J. Marangos, Nature 397 (1999) 559.
[9] M. Scalora, J. Flynn, S.B. Reinhardt, R.L. Fork, M.D. Tocci, M.J. Bloemer, C.M. Bowden, H.S. Ledbetter, J.J. Bendickson, J.P. Dowling, J.W. Haus, Phys. Rev. E 54 (1996) R1078.
[10] J.P. Dowling, M. Scalora, M.J. Bloemer, C.M. Bowden, J. Appl. Phys. 75 (1994) 1896.
[11] J.P. Dowling, C.M. Bowden, Phys. Rev. A 46 (1992) 612.
[12] M. Megens, J.E.G.J. Wijnhoven, A. Lagendijk, W.L. Vos, Phys. Rev. A 59 (6) (1999) 4727.
[13] R. Uitham, B.J. Hoenders, Opt. Commun. 262 (2006) 211.
[14] S. Shen, K.E. Oughstun, J. Opt. Soc. Am. B 6 (5) (1989) 948.
[16] P. Yeh, A. Yariv, J. Opt. Soc. Am. 67 (1977) 423.
[17] M. Centini, C. Sibilia, M. Scalora, G. D'Aguanno, M. Bertolotti, M.J. Bloemer, C.M. Bowden, I. Nefedov, Phys. Rev. E 60 (4-B) (1999) 4891. Part B.
[18] A.P. Juzakov, Math. USSR Sbornik 26 (2) (1975) 165.
[19] I.A. Aizenberg, A.P. Juzakov, Integral Representations and Residues in Multidimensional Complex Analysis, American Mathematical Society, 1983.